ChemComm

FEATURE ARTICLE

View Article Online
View Journal

Cite this: DOI: 10.1039/d2cc05660g

Redox-active polyimides for energy conversion and storage: from synthesis to application

Taehyung Kim, †[a] Jiyoung Lee, †[a] Namhee Kim, †[a] Sujin Lee,†[b] Minsu Gu †*[b] and Byeong-Su Kim †*[a]

Received 18th October 2022,
Accepted 29th November 2022

DOI: 10.1039/d2cc05660g

rsc.li/chemcomm

As the demand for next-generation electronics is increasing, organic and polymer-based semiconductors are in the spotlight as suitable materials owing to their tailorable structures along with flexible properties. Especially, polyimide (PI) has been widely utilised in electronics because of its outstanding mechanical and thermal properties and chemical resistance originating from its crystallinity, conjugated structure and π–π interactions. PI has recently been receiving more attention in the energy storage and conversion fields due to its unique redox activity and charge transfer complex structure. In this review, we focus on the design of PI structures with improved electrochemical and photocatalytic activities for use as redox-active materials in photo- and electrocatalysts, batteries and supercapacitors. We anticipate that this review will offer insight into the utilisation of redox-active PI-based polymeric materials for the development of future electronics.

1. Introduction

As the demand for next-generation wearable electronics and robotics is ever-increasing,[1] thin-film-based flexible electronic devices that can be bent, folded, twisted, compressed and stretched into arbitrary shapes are receiving significant attention owing to their high electrical and mechanical performances.[2] Since traditional rigid metal-oxide-semiconductors have limited softness and flexibility, organic semiconducting materials based on soft, lightweight and molecularly tailorable small molecules and polymers are essential prerequisites toward realising next-generation flexible electronics.[3] Therefore, various approaches utilising polymeric substrates comprising plastics, elastomers, paper and textiles have been studied for the fabrication of flexible and conductive electrodes[4] hybridised with multidimensional nanomaterials, ferroelectric polymers and thermoelectric materials.[5–8]

Among the promising organic-based electronic device materials, polyimide (PI) is drawing much attention because of its superior thermo-oxidative stability, high mechanical strength,

[a] Department of Chemistry, Yonsei University, 50 Yonsei-ro, Seoul 03722, Republic of Korea. E-mail: bskim19@yonsei.ac.kr
[b] Department of Chemical Engineering (BK21 FOUR), Dong-A University, Busan 49315, Republic of Korea. E-mail: sbgms@dau.ac.kr
† All authors contributed equally to this work.

Taehyung Kim

Taehyung Kim received his BS and PhD from the Department of Energy Engineering at the Ulsan National Institute of Science and Technology (UNIST), Republic of Korea, in 2017 and 2022 under the supervision of Prof. Byeong-Su Kim. He is currently working as a postdoctoral researcher in Prof. Byeong-Su Kim's group in Yonsei University. His research interests include the design and synthesis of redox-active polyimide materials for lithium-ion batteries and photocatalyst.

Jiyoung Lee

Jiyoung Lee is currently a PhD student in Prof. Byeong-Su Kim's group in the Department of Chemistry at Yonsei University. She received her BS and MS from the Department of Chemistry at Soongsil University, Republic of Korea, in 2018 and 2020 under the supervision of Prof. Ik-Soo Shin. Her research interests include nanomaterials and polymers for energy conversion.

unique electrical properties and high solvent resistance. Owing to these outstanding properties originating from its crystallinity, conjugated structure and π–π interactions, PI has been applied in high-tech industries such as aerospace, electronics and optics (Fig. 1).[9] Recently, the insulating property of PI as an encapsulating layer has been used to protect devices from external attrition.[10]

New approaches for PI applications have been emerging in the fields of energy conversion and storage systems based on PI's donor–acceptor structure and redox activity. Electron-rich amine and electron-deficient anhydride moieties used to construct donor–acceptor structures enable facile charge transfer in energy conversion and storage systems. In addition, they are beneficial for charge separation as the highest occupied molecular orbital (HOMO) and lowest unoccupied molecular orbital (LUMO) are located at the donor and acceptor positions, respectively;[11] the energy band diagram demonstrates that the bandgap of PI can be tailored *via* comonomer tuning in the visible-light range of 1.9–3.0 eV (Fig. 1(b)).[12–15] As a result, several research groups have exploited semiconducting PI for various photocatalytic energy conversion reactions.[16–19] Furthermore, PI is considered to be an excellent redox-active polymer that can store electric energy *via* enolization reactions of its carbonyl groups with the metal ions of elements such as Li and Na (Fig. 1(c)).[20,21] As the performance of polymer electrode materials depends on the functional groups, PI has been studied as both a cathode and anode material. In addition, the operating voltage can be readily tuned by selecting a suitable precursor combination to control the conjugation length or electronegativity.[22,23]

Over the century since the development of PI, its properties and synthetic methods have been reviewed in the context of various applications. In contrast, the aim of this review is to cover its use in energy conversion and storage applications along with the recent progress in the synthetic methods and topological control used to produce PI (Fig. 2). In the first section, we discuss diverse imidization reactions in various synthetic environments and the progress in topological control

Namhee Kim

Namhee Kim is currently an PhD student under the guidance of Prof. Byeong-Su Kim in the Department of Chemistry at Yonsei University. She received her BS from the Department of Chemistry at Chungnam National University, Republic of Korea, in 2020. Her research interests include nanomaterials and polymers for energy conversion.

Sujin Lee

Sujin Lee is currently a MS student in Prof. Minsu Gu's group in the Department of Chemical Engineering at Dong-A University, Republic of Korea. She received her BS degree from the Department of Chemical Engineering at Dong-A University, in 2022. Her research interests include photo and electrocatalytic nanomaterials for energy conversion.

Minsu Gu

Minsu Gu is an Assistant Professor in the Department of Chemical Engineering at Dong-A University, Republic of Korea. He received his BS from the School of Nano-Bioscience and Chemical Engineering at Ulsan National Institute of Science and Technology (UNIST), Republic of Korea, in 2013, and his PhD from the Department of Energy Engineering at UNIST in 2018 under the supervision of Prof. Byeong-Su Kim. He was a postdoctoral researcher in Dr Allen J. Bard's group in the Department of Chemistry at the University of Texas at Austin. His research interests include the electrochemistry of functional nanomaterials and polymers for energy conversion and storage applications.

Byeong-Su Kim

Byeong-Su Kim is a Professor in the Department of Chemistry at Yonsei University, Republic of Korea. He received his BS and MS in Chemistry from Seoul National University and his PhD in Chemistry from the University of Minnesota, Twin Cities, in 2007. After his postdoctoral research at MIT, he started his independent career at UNIST in 2009 and moved to Yonsei University in 2018. His research group investigates a broad range of topics in macromolecular chemistry to study novel polymer and hybrid nanomaterials, including the molecular design and synthesis of self-assembled polymers and hybrid nanostructures.

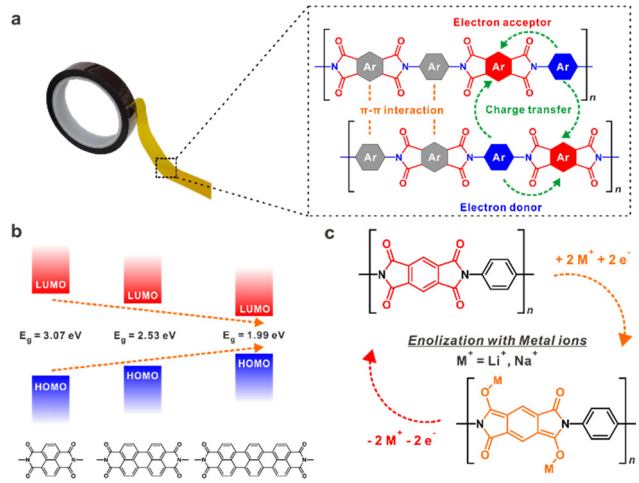

Fig. 1 (a) An image of PI product Kapton tape as a representative PI structure with inter- and intramolecular interactions (the electron donor–acceptor structure, charge transfer and π–π interactions). (b) A diagram of the controllable bandgap of PI comprising various structures. (c) The redox-active properties of PI with metal ions *via* enolization.

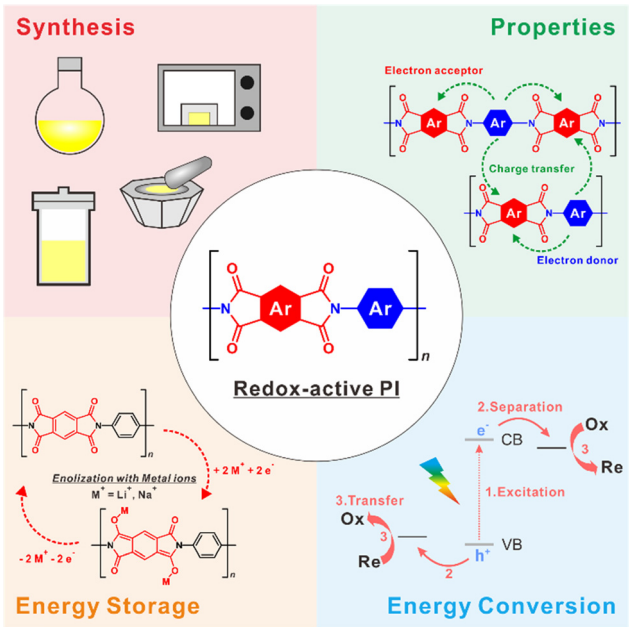

Fig. 2 An overview of the review of redox-active PI: synthesis, properties, energy conversion and storage.

from linear to porous crystalline networks. Following that, the applications of PIs for energy conversion and storage are covered based on the redox activity of PI. The review is concluded with a summary of the effect of polymer structure and composition on the redox activity of PI with future perspectives.

2. PI synthesis and structure

2.1. Synthetic methods

Since the first synthesis of PI through intramolecular polycondensation in 1908,[24] various synthetic approaches using a diverse array of aromatic compounds have been developed that provided excellent physical properties and conjugated structures. The two-step condensation reaction between anhydride and amine precursors is the most conventional synthetic method. In this process, poly(amic acid) (PAA) is initially formed, followed by intramolecular imidization (Fig. 3(a)).[25] In the first step, amine attacks the carbonyl group of anhydride monomer, which opens the anhydride ring and forms the PAA structure. Imidization of PAA then occurs under high temperature, typically above 200 °C, which drives the thermodynamically favoured intramolecular condensation reaction. In order to reduce the imidization temperature, chemical imidization was developed using a dehydration agent and a basic catalyst.[26]

Isocyanate instead of amine has been successfully used as a precursor for the synthesis of PI. Meyer *et al.* proposed the mechanism with the formation of a seven-membered ring and carbon dioxide (CO_2) as the intermediate and the by-product, respectively (Fig. 3(b)).[27] However, based on the observation of a low conversion rate under dry conditions, Carleton *et al.* proposed another mechanism with the hydrolysis of isocyanate (Fig. 3(c)).[28] Depending on the degree of hydrolysis, amine or urea was generated, followed by a condensation reaction with anhydride.

Alternative synthetic methods without using organic solvents such as solid-state and aqueous synthesis have been proposed because the aforementioned methods are mostly based on solution-processing using toxic organic solvents such as *N*,*N*-dimethylformamide (DMF), *N*-methyl-2-pyrrolidone (NMP) or *N*,*N*-dimethylacetamide (DMAc) (Fig. 3(e)). Scalable and eco-friendly PI synthesis based on solid-state condensation has been carried out *via* the thermal treatment of physically mixed amine and anhydride monomers at a high temperature in the absence of solvents.[29] At such a high reaction temperature, the anhydride precursor melts and reacts with the nearby amine monomers, followed by the formation of an oligomeric structure and further imidization. In addition, Yuan and co-workers reported a microwave-assisted heating method for the solid-state synthesis of PI in a very short time as using a microwave absorber such as copper(II) oxide (CuO) rapidly increases the temperature.[30] Recently, mechanochemistry has been applied to synthesize PI from diverse anhydride and amine precursors.[31] PAA was constructed *via* a mechanochemical reaction using ball milling and subsequent thermal imidization (Fig. 3(e)).

In another eco-friendly synthetic method, Chiefari *et al.* synthesized PI under aqueous conditions using carboxylate and ammonium salt intermediates (Fig. 3(d));[32] the anhydride precursor hydrated first to form tetracarboxylic acid, followed by the formation of a carboxylate-ammonium salt. Subsequently, the salt was dehydrated and imidized *via* thermal treatment after drying. Recently, Unterlass *et al.* demonstrated the one-pot synthesis of PI in aqueous media through a hydrothermal method under high temperature and pressure conditions in a closed vessel (Fig. 3(d)),[33–35] where crystalline PI was formed *via* a dissolution–polymerization–crystallisation process (Fig. 4). Imidization in aqueous media is possible

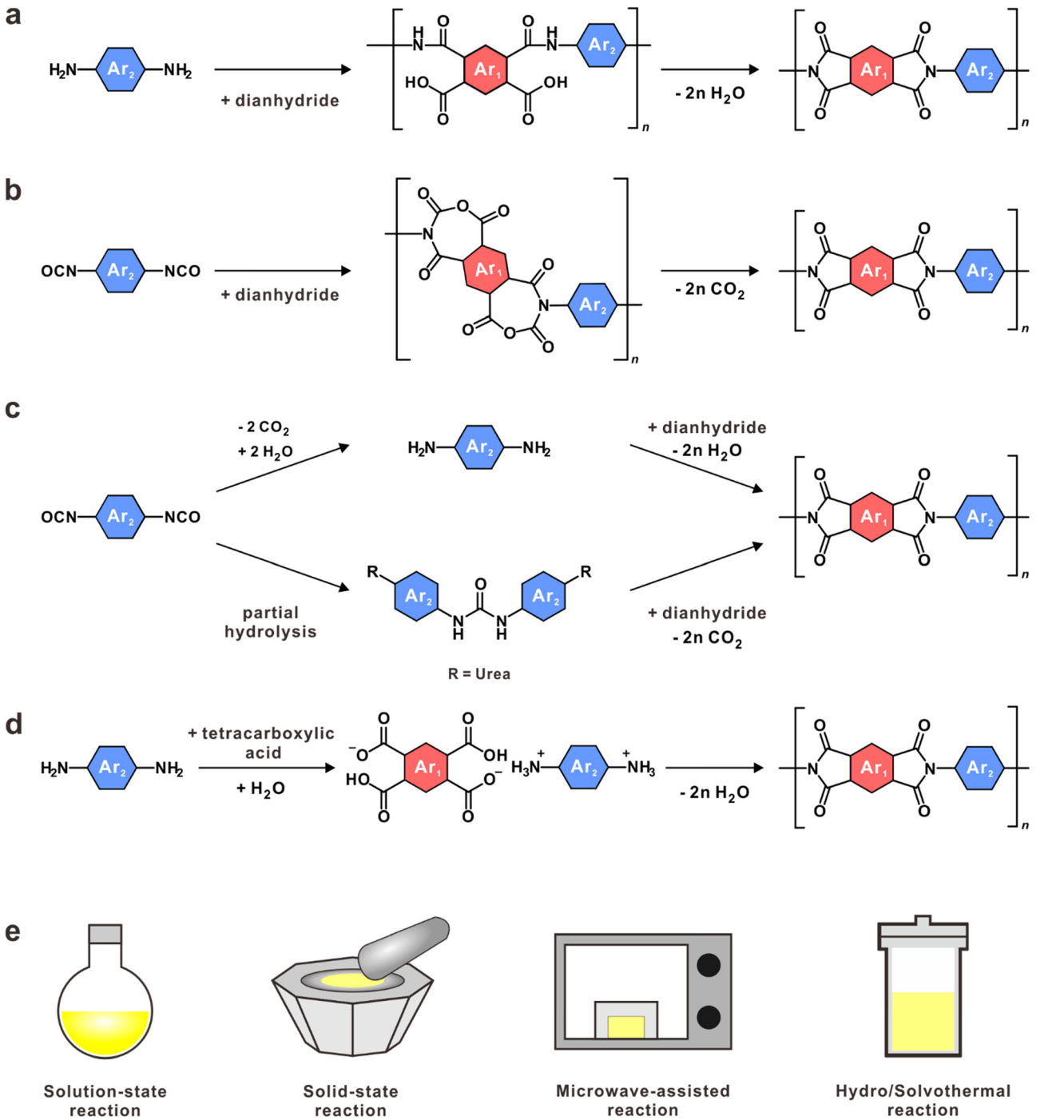

Fig. 3 (a–d) Representative synthetic approaches for PI *via* various reaction pathways and (e) the diversity of apparatus used in the production of PI.

because the physicochemical properties of water change significantly as the hydrogen bonding of the water network is broken under hydrothermal conditions.[36] In particular, the density and viscosity of water significantly decrease under hydrothermal conditions, thus affecting diffusion-controlled chemical reactions. Furthermore, the dielectric constant of water decreases continuously and even matches that of common organic solvents under ambient conditions.[37] More importantly the ionic products of water increase with increasing temperature, thus accelerating the rate of acid- and base-catalysed reactions.[38]

2.2. The structure and topology of PI

Since the successful commercialisation of PI-based Kapton film, linear PIs have been produced using various dianhydride and diamine monomers (Fig. 5).[39,40] However, there is a limitation in fabricating aromatic PIs through solution-processing due to strong interactions between the polymer chains. In this

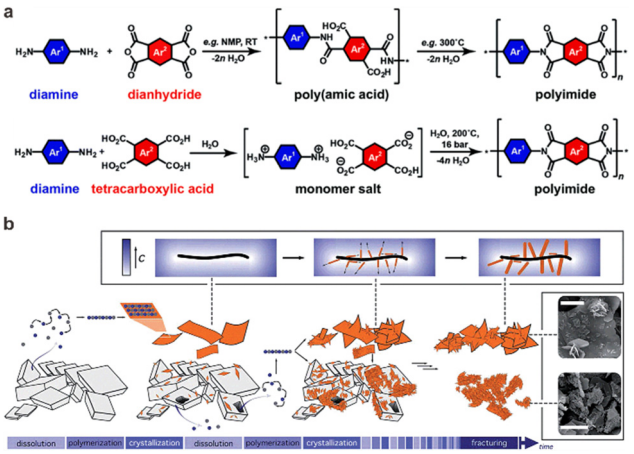

Fig. 4 (a) The classical and hydrothermal pathways for synthesizing PI. Reproduced with permission from ref. 34, copyright 2015, The Royal Society of Chemistry. (b) Crystalline PI formation mechanism during hydrothermal polymerization. Reproduced with permission from ref. 33, copyright 2014, The Royal Society of Chemistry.

context, various approaches have been suggested to overcome this issue, including introducing flexible linkages or aliphatic units in the polymer backbone,[41–43] introducing side groups to hinder molecular packing and crystallization[44–46] and introducing asymmetric monomers to suppress coplanar structures.[47–52]

This topological control has been further extended with multifunctional precursors (Fig. 5). Firstly, dendritic or hyperbranched structures are constructed through a stepwise reaction using AB_2-type monomers.[53] For example, Shu and coworkers reported the synthesis of dendritic poly(ether imide) through aromatic nucleophilic substitution and imidization between 1-(4-aminophenyl)-1,1-bis(4-hydroxyphenyl)ethane with 3-nitro-*N*-phenylphthalimide and 3-nitrophthalic anhydride.[54,55] Kakimoto and coworkers reported the synthesis of hyperbranched poly(ether imide) through the imidization of an AB_2-type poly(amic acid) ester monomer prepared from 3,5-dimethoxyphenol and 4-nitrophthalonitrile.[56–58] Furthermore, the imidization reaction of PAA from A_2 and B_3 monomers such as 1,3,5-tris(4-aminophenyl)benzene, triaminotriphenylamine, melamine, melem, 1,3,5-tri(1,3-dioxo-1,3-dihydroisobenzofuran-5-yloxy)benzene and mellitic anhydride has been reported.[59,60] Combination of these A_2 and B_3-type monomers constructs cross-linked porous structures that enhance the accessibility of reactants such as Li^+ or redox substances.[61–65] Although microporous PI extended the utility range of the latter as a membrane for gas and energy storage purposes, the limitation still exists due to its low specific surface area and non-uniform pore size.

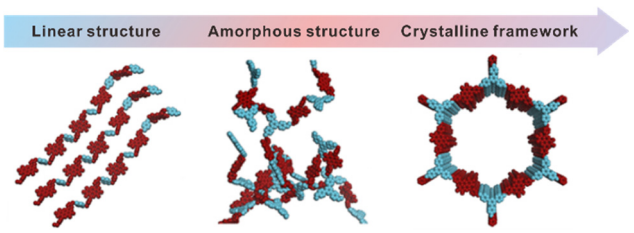

Fig. 5 The various topological structures of PI. Reproduced with permission from ref. 113, copyright 2021, American Chemical Society.

Recently, 2D and 3D crystalline porous systems known as covalent organic frameworks (COFs) with a confined and uniform pore size and high surface area have been shown to overcome the limitations of PI structures (Fig. 5). Yan and co-workers reported the synthesis of 2D and 3D PI-COFs with triamine and tetraamine precursors *via* solvothermal reactions using organic solvents and catalysts for the first time.[66,67] Since then, most PI-COFs have been synthesized *via* the solvothermal method because reversible bond formation and deformation are essential for constructing PI structures with high crystallinity. Moreover, it is related to the solubility of intermediates and the pK_a values of the reaction media with an appropriately targeted catalyst. As a result, PI-COFs of various topologies have been synthesized by using the solvothermal method with varying precursor combinations.[68] Recently, we reported the eco-friendly synthesis of PI-COFs through the hydrothermal method by exploiting triphenylene-2,3,6,7,10,11-hexacarboxylic acid in combination with three different aromatic diamines.[69] Their crystalline structures, especially 3D stacking structures, were affected by the solubility of oligomeric structures, which act as seeds for nucleation that creates the most thermodynamically stable eclipsed stacking structure under hydrothermal conditions. In contrast, insoluble oligomeric structures are separated with precursors, which limits further growth and constructs kinetically favoured staggered stacking structures (Fig. 6). In addition, Lotsch and coworkers recently reported the eco-friendly ionothermal synthesis of PI-COFs with a eutectic mixture of sodium chloride, potassium chloride and zinc chlorides.[70]

3. Application of PIs to energy conversion and storage

3.1. Energy conversion

3.1.1 PI photocatalysts. To improve the photocatalytic activity of PI-based photocatalysts, it is important to (i) engineer the HOMO/LUMO position and bandgap, (ii) separate the charge carriers effectively and (iii) increase the surface activity sites. In this section, we introduce the various strategies for producing PI-based photocatalysts and classify them into three types while also revealing the relationship between their structure and photocatalytic ability. The π-conjugated sp^2-carbon network of PI can be extended to narrow the bandgap, thereby improving solar utilisation efficiency owing to the recruitment of more photons in the visible-light region. Furthermore, the LUMO energy level is lowered by electron-withdrawing groups as a result of attracting electrons out of the π-conjugated backbone.[11,71] In recent years, the coupling of electron-rich donors and electron-deficient acceptors has become widely known as a strategy for tuning the energy band structure.[16–19,72,73] The bandgap of PI can be modulated in the visible-light range (1.9 to 3.0 eV) by changing the reaction temperature and

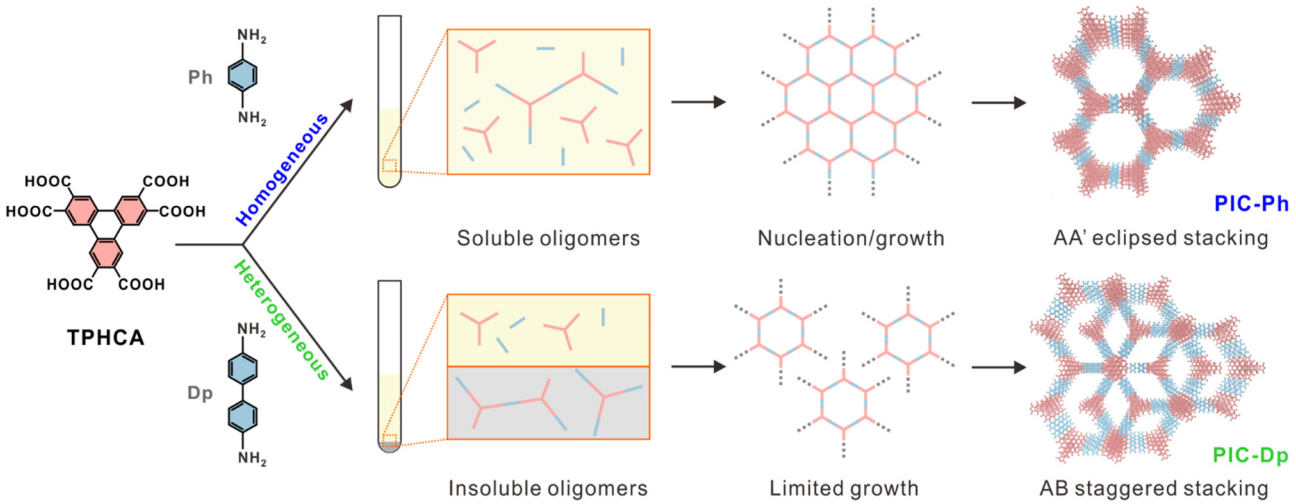

Fig. 6 The construction mechanism for PI-COFs under hydrothermal conditions. Reproduced with permission from ref. 69, copyright 2021, Wiley-VCH GmbH.

comonomer structure.[12–14,64,74] The donor–acceptor structure of PI usually consists of electron-rich amine and electron-deficient anhydride moieties, respectively, leading to its high chemical tunability. Theoretical calculations indicate that the HOMO and LUMO of PI are located on the amine and anhydride moieties, respectively.[11]

Zou and co-workers produced a crystalline PI-based photocatalyst for the hydrogen evolution reaction (HER) by mixing melamine with pyromellitic dianhydride (PMDA) at a high condensation temperature.[75] UV-vis absorption spectra of the photocatalyst indicate that the bandgap of PI decreased from 3.39 to 2.56 eV when the reaction temperature was increased from 250 to 350 °C. The decrease in bandgap originated from the enhanced degree of polymerization in the conjugated system. As a result, it was possible to produce more charge carriers for proton reduction and sacrificial oxidation. The obtained samples produced hydrogen from water upon visible light illumination while Pt and triethanolamine acting as a cocatalyst and an electron donor, respectively. The PI catalyst with a moderate bandgap generated the maximum H_2 evolution activity of 150 and 15.2 μmol h^{-1} under UV and visible-light irradiation, respectively, thus indicating the importance of bandgap engineering for promoting photocatalytic activity.

Shiraishi and coworkers fabricated graphitic carbon nitride (g-C_3N_4) photocatalysts containing pyromellitic diimide (PDI) for hydrogen peroxide (H_2O_2) production from water and molecular oxygen (Fig. 7(a)).[12] Incorporating electron-deficient aromatic diimide units positively shifted the valence band (VB) potential of the photocatalysts due to their high electron affinity while maintaining sufficient conduction band (CB) potential for the two-electron reduction of O_2 (Fig. 7(b)). Consequentially, the photocatalysts successfully produced H_2O_2 by oxidizing water under sunlight irradiation. Thus, g-C_3N_4 engineered by incorporating aromatic diimide units is a safe and green photocatalyst capable of sustainable H_2O_2 evolution.

To promote the charge carrier separation of PI-based photocatalysts, active groups can be introduced into the building blocks of an existing architecture. Another strategy for extending the lifetime of the charge carriers is heterojunction engineering through combining PI with other materials.[76–80] In this context, Yan *et al.* prepared a novel organic–inorganic composite (PI/$Zn_{0.25}Cd_{0.75}S$) *via* a template-free hydrothermal method.[81] Electrochemical impedance spectroscopy (EIS) was employed to investigate its charge separation and transfer efficiency. The impedance of PI/$Zn_{0.25}Cd_{0.75}S$ was smaller than that of pristine PI and neat $Zn_{0.25}Cd_{0.75}S$, indicating that the interface layer resistance of the composite was lower than that of pure PI (Fig. 7(c)). The EIS results demonstrate that the heterojunction facilitates the charge separation and transfer of photogenerated charge carriers on the photocatalytic surface. Consequently, PI/$Zn_{0.25}Cd_{0.75}S$ showed improved photocatalytic activity for dye degradation under visible-light irradiation compared to PI or $Zn_{0.25}Cd_{0.75}S$ alone. This can be ascribed to the synergistic effect of interfacial electronic interaction and efficient migration of photogenerated charge carriers due to suitable band structure leading to improved charge separation (Fig. 7(d)).

Hu *et al.* designed a cadmium sulfide (CdS)/PI heterojunction photocatalyst *via* the *in situ* growth of CdS nanoparticles on ultrathin nanosheets of PI through a one-pot solvothermal method.[82] The charge-transfer mechanism of the direct Z-scheme heterojunction was demonstrated by using time-resolved fluorescence decay. While photoluminescence suggests only the primary pathway is involved in the recombination and dissipation of charge carriers, time-resolved fluorescence decay spectroscopy can provide details of the dynamic characteristics of the charge-transfer process. The results reveal that the lifetime of the excited state of the CdS/PI composite was shorter than that of pure PI and CdS, which can be attributed to the promotion of electron transport by processes such as non-radiative energy transfer. The direct Z-scheme pathway was further verified *via*

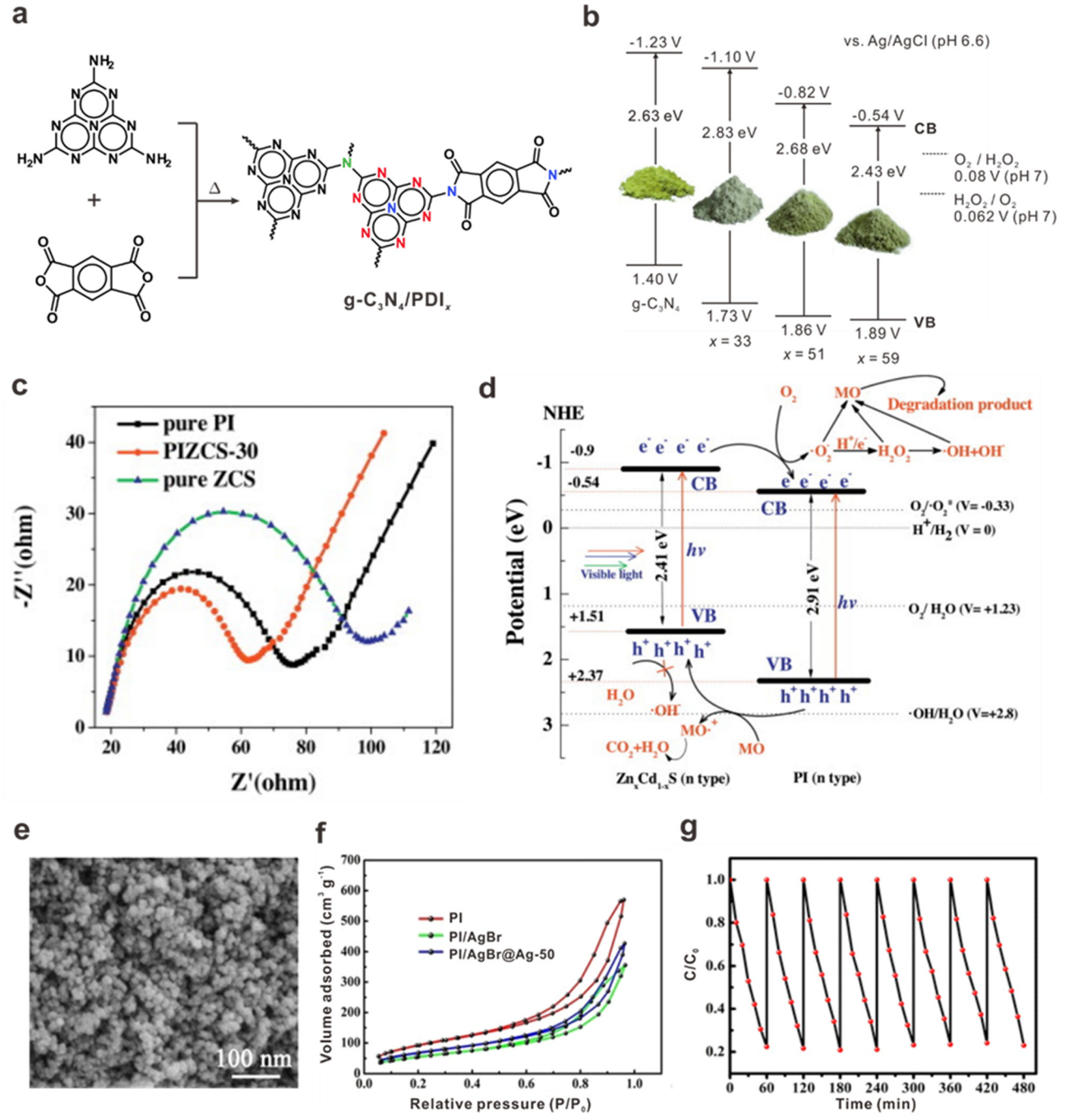

Fig. 7 Representative examples for PI-based photocatalysts. (a) The reaction scheme for the synthesis of g-C_3N_4/perylene diimide (PDI). Reproduced with permission from ref. 12, copyright 2014, John Wiley & Sons, Inc. (b) Electronic band structures of g-C_3N_4 and g-C_3N_4/PDI. Reproduced with permission from ref. 12, copyright 2014, John Wiley & Sons, Inc. (c) Electrochemical impedance spectra of PI, ZnCdS and a PI/ZnCdS composite. Reproduced with permission from ref. 81, copyright 2015, Elsevier. (d) The proposed mechanism for the photocatalytic dye degradation on the PI/ZnCdS composite under visible light irradiation. Reproduced with permission from ref. 81, copyright 2015, Elsevier. (e) A scanning electron microscopy image, (f) adsorption–desorption isotherms and (g) cycling experiments for oxytetracycline degradation *via* a PI/AgBr@Ag aerogel. Reproduced with permission from ref. 84, copyright 2019, John Wiley & Sons, Inc.

in situ X-ray photoelectron spectroscopy (XPS) measurements under visible-light irradiation. The results demonstrate that the photoexcited electrons in PI were transferred to CdS, revealing the presence of a direct Z-scheme heterojunction in the CdS/PI composite. In turn, the maximum H_2 production rate of CdS/PI reached 613 μmol h^{-1} g^{-1} under visible-light irradiation, which is around five times higher than that of neat CdS.

An indirect Z-scheme heterojunction *via* an electron mediator has also been designed in PI-based photocatalysts. Guo *et al.* constructed an all-solid silver phosphate (Ag_3PO_4)/nitrogen-doped

graphene (NG)/PI composite in which NG acts as an electron mediator for efficient electron transfer from the CB of Ag_3PO_4 to the VB of PI.[83] The prepared photocatalyst presented high photocatalytic performance for pollutant degradation. Superoxide radicals and hydroxyl radicals detected *via* electron paramagnetic resonance spectroscopy were the active species during the photocatalytic process. They also verified that the heterojunction follows the Z-scheme because the CB energy level of Ag_3PO_4 was less negative for O_2 reduction to produce superoxide radicals and the VB position of PI was less positive for H_2O oxidation to produce hydroxyl radicals. Furthermore, electron transfer not only enhanced charge transfer but also suppressed the photocorrosion of Ag_3PO_4, as demonstrated *via* photocurrent response analysis.

Nanostructure engineering provides another powerful strategy for shortening the carrier capture pathway and increasing the active surface area, leading to enhance photocatalytic efficiency. The development of PI-based photocatalysts with a single or a few layers of porous structures is highly desirable for promoting photocatalytic activity because most PI-based photocatalysts have a low specific surface area (below 20 $m^2\ g^{-1}$). Zhao *et al.* reported PI-based aerogels for the degradation of oxytetracycline under visible-light irradiation.[84] A PI/silver bromide (AgBr)@Ag composite aerogel was prepared as a photocatalyst by dispersing AgBr@Ag nanoparticles uniformly on a PI aerogel (Fig. 7(e)). The resulting PI/AgBr@Ag aerogel photocatalyst showed excellent photocatalytic activity for the degradation of oxytetracycline with a degradation rate of 99.8% within 240 min under visible-light irradiation. Moreover, the rate constant was 0.025 min^{-1}, which is 2.6 and 6.9 times higher than that of AgBr@Ag nanoparticles or PI aerogel alone, respectively. In addition, the PI/AgBr@Ag aerogel photocatalyst exhibited excellent cycling stability due to the high mechanical strength and 3D network of PI aerogel (Fig. 7(g)). The high photoactivity was not only attributed to its high specific surface area (191 $m^2\ g^{-1}$) but also to the Z-scheme heterojunction structure (Fig. 7(f)). Similarly, Zhao *et al.* prepared a 3D porous PI aerogel photocatalyst with a high specific surface area of 97 $m^2\ g^{-1}$ *via* a sol–gel method.[85] The PI aerogel photocatalyst with Ag and methanol as a cocatalyst and an electron donor, respectively, provided a high hydrogen evolution rate of 166.1 mmol $h^{-1}\ g^{-1}$ under visible-light irradiation, which was eight times higher than that of the pristine PI aerogel without a cocatalyst (Table 1).

3.1.2 Photoelectrochemical cells. As mentioned earlier, the HOMO and LUMO of PI are located in the amine and dianhydride moieties, respectively, which ensures the characteristics of semiconducting polymer with improved charge separation capability. Furthermore, aromatic PI has significantly enhanced photoelectrochemical properties due to high visible-light response and electrical conductivity compared with other organic compounds. More importantly, PI with a high glass-transition temperature exhibits excellent chemical resistance, thermal stability and mechanical strength, thereby providing good adhesion between aromatic PI and a conductive substrate leading to long-term stability. In this section, we summarise the strategies for enhancing the light absorption and transfer of photogenerated electrons and holes by PI, while obtaining a higher and more stable photocurrent signal.

Conducting polymers with nanoparticles are highly applicable for high-density energy storage and conversion strategies. Among the treatment methods for increasing the incident-photon-to-current efficiency (IPCE), doping conducting polymer with transition metals, metal oxides and/or carbonaceous materials have been suggested to provide practical and effective solutions. Wang *et al.* doped poly(perylene tetracarboxylic imide) (PPI) in nano-TiO_2/ITO film with CdSe nanoparticles for use as a photoelectrode, which significantly increased its monochromatic incident IPCE.[90] Doping with CdSe nanoparticles improved the absorbance in the visible-light range by providing an interface for separating electron–hole pairs and a channel for transferring charge carriers for promoting photovoltaic capability. Accordingly, the photocurrent of CdSe-nanoparticle-doped TiO_2 film was nearly three times higher than that of non-doped film.

Wang and coworkers demonstrated an efficient approach for the design of PI-based composites with graphene oxide (GO) to overcome the poor solubility of PI in common organic

Table 1 Representative examples of PI-based photocatalysts

Materials	Applications	Role of PI	Photocatalytic efficiency	Ref.
g-C_3N_4/PI	H_2O_2 production	Bandgap modulation	H_2O_2 production = 30 μmol	12
g-C_3N_4/biphenyl diimide	H_2O_2 production	Charge separation	H_2O_2 production = 11.6 μmol	86
g-C_3N_4/pyromellitic diimide	H_2O_2 production	Charge separation	H_2O_2 production = 60 μmol	87
g-C_3N_4/mellitic triimide	H_2O_2 production	Charge separation	H_2O_2 production = 50 μmol	88
Self-assembled PI supermolecule	Hydrogen evolution	Charge transfer	H_2 production rate = 1640 μmol $h^{-1}\ g^{-1}$	89
CdS/PI	Hydrogen evolution	Charge separation	H_2 production rate = 613 μmol $h^{-1}\ g^{-1}$	82
PI/Ag aerogel	Hydrogen evolution	Enhanced charge mobility and large specific area	H_2 production rate = 166.1 μmol $h^{-1}\ g^{-1}$	85
PI/$Zn_{0.25}Cd_{0.75}S$	Dye degradation	Charge separation	Degradation rate = 100%	81
Ag_3PO_4/N-doped graphene/PI	Microcystin-LR degradation	Charge separation and migration	Degradation ratio = 94.4%	83
PI/AgBr@Ag	Oxytetracycline degradation	Charge separation and large specific area	Degradation rate = 99.8%	84

PI, polyimide; g-C_3N_4, graphitic carbon nitride; Ag_3PO_4, silver phosphate; CdS, cadmium sulphide.

solvents.[91] Covalent interactions between the poly(amic acid)s and the carboxylic acid group of GO *via* amide linkage prevented the aggregation of GO sheets during the thermal imidization process, resulting in its uniform dispersion in the PI matrix. The resulting composites had high thermal resistance as well as excellent solubility in various organic solvents

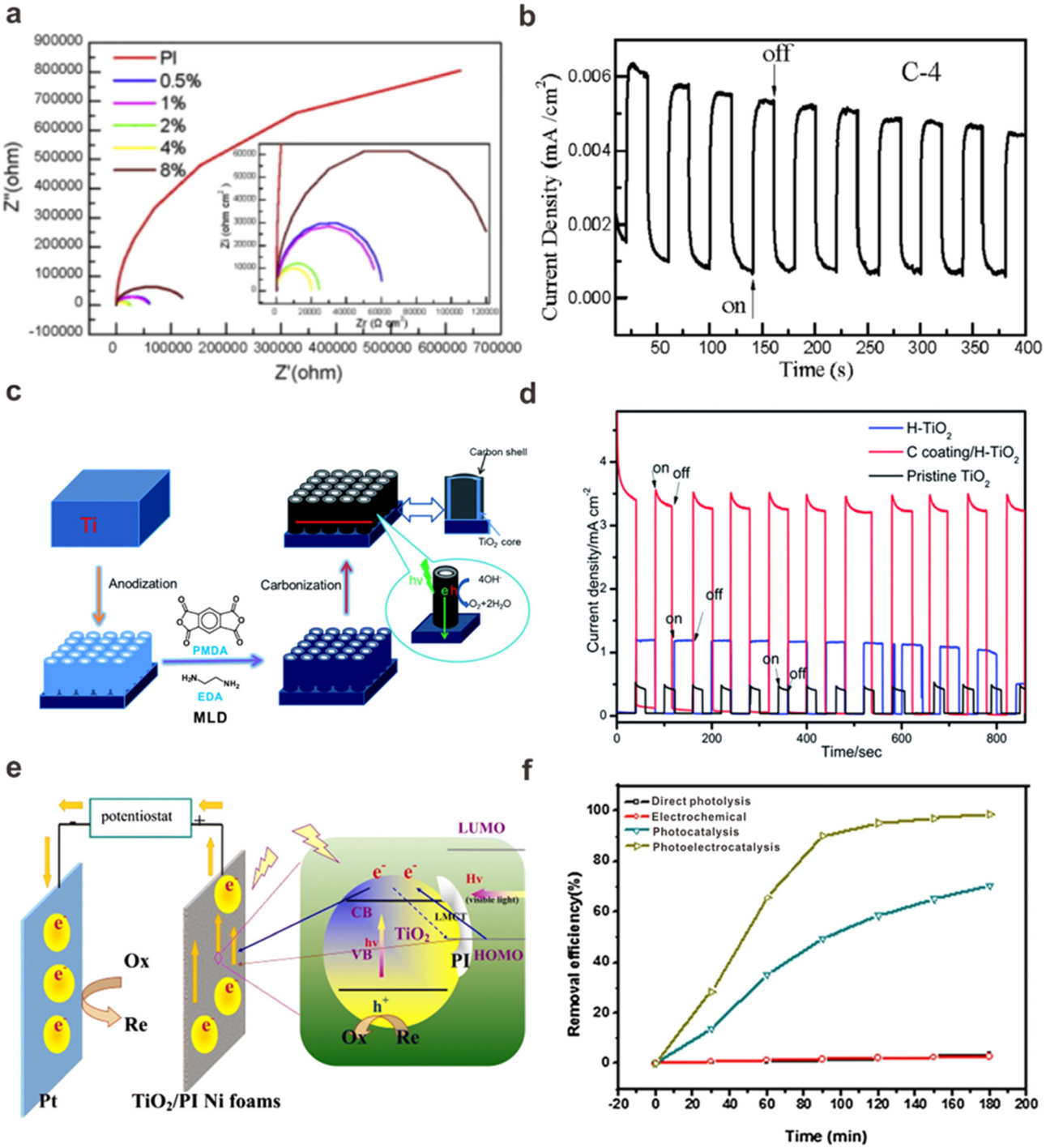

Fig. 8 (a) Nyquist plots of the electrochemical impedance spectra for PI and its composite films. Reproduced with permission from ref. 91, copyright 2014, Elsevier. (b) Photocurrent response for PI composite film under on/off light irradiation. Reproduced with permission from ref. 91, copyright 2014, Elsevier. (c) A schematic representation of the coating process of vertically oriented TiO_2 nanotube arrays (TNTAs) with an ultrathin carbon film. Reproduced with permission from ref. 92, copyright 2014, The Royal Society of Chemistry. (d) Chronoamperometric curves at a potential of 0.23 V (*vs.* AgCl/Ag) under irradiation for light on/off cycles. Reproduced with permission from ref. 92, copyright 2014, The Royal Society of Chemistry. (e) A schematic illustration of the photoelectrochemical oxidation of organic pollutants using a TiO_2/PI/Ni foam photoanode under visible-light irradiation. Reproduced with permission from ref. 93, copyright 2018, Springer Nature. (f) Various processes for methylene blue (MB) degradation using TiO_2/PI/Ni foam photoanode. Reproduced with permission from ref. 93, copyright 2018, Springer Nature.

such as DMF, DMAc and NMP. In particular, the GO played a crucial role in the electron transfer process under illumination and controlled the conductivity of the composite film. While the PI composite film containing 4 wt% GO (*i.e.* C-4) achieved the lowest resistance, increasing the GO content to 8% decreased the conductivity and thus the photoelectrical response (Fig. 8(a)). Furthermore, the 4 wt% GO/PI composite film showed good reversible photocurrent responses over several on/off light illumination cycles (Fig. 8(b)).

PI-based composites have been widely employed for water splitting and pollutant remediation. Tong and coworkers fabricated an ultrathin nitrogen-doped carbon film coated on the walls of highly ordered TiO_2 nanotube arrays (TNTAs) *via* carbonisation of PI film deposited by using molecular layer deposition for water splitting (Fig. 8(c)).[92] Pristine TiO_2 was simultaneously converted to hydrogenated TiO_2 during the carbonisation process, thereby protecting the regular morphology of the TNTAs. In the hydrogenated TNTAs without the carbon film coating, Ti^{3+} in the aqueous electrolyte was unstable because it could be oxidized by oxygen dissolved in the water. Meanwhile, the surface of the TNTAs coated with a carbon film enhanced solar absorption and electron–hole pair generation (Fig. 8(d)). While the photogenerated holes moved to the electrode–electrolyte interface and participated in the oxygen evolution reaction (OER), the electrons that had migrated to the substrate were transferred to the counter electrode and participated in the HER. Moreover, the nitrogen-doped carbon film provided a high proportion of catalytic active sites for OER. The core/shell nanostructure with a controllable shell thickness also provided a larger heterojunction interface that suppressed the recombination of photogenerated electrons and holes. Consequently, the nitrogen-doped carbon film coated on TNTAs exhibited an improved photocurrent under solar light irradiation of approximately five-fold compared to pristine TiO_2.

Lei *et al.* developed a TiO_2/PI/Ni foam photoanode for MB degradation by dispersing a porous nanostructured TiO_2 film in a PI/Ni foam substrate.[93] Although Ni foam possesses many advantages owing to its large surface area, evenly distributed pore size and high conductivity, it is rarely used as a conductive support due to its facile oxidation during the photoelectrochemical reaction. To suppress this, a protective layer was produced on the surface by filling the Ni foam with a polymer. Furthermore, the TiO_2–PI charge-transfer complex exhibited a high visible-light response and electroactivity resulting from the high proportion of aromatic moieties in PI. Consequentially, the prepared photoanode showed broad visible-light absorption, excellent photoinduced current propagation and high photoelectrochemical efficiency toward degrading MB under simulated solar light irradiation (Fig. 8(f)). Electrons that transferred from the VB to the CB of TiO_2 under UV light irradiation migrated to the Pt electrode due to the external bias potential (Fig. 8(e)). Subsequently, the holes generated on the surface of the TiO_2/PI/Ni foam photoanode and electrons produced on the surface of the Pt electrode could then react with the organic pollutant. This superior photoelectrochemical performance could be attributed to the TiO_2–PI charge-transfer complex inducing high separation efficiency of photogenerated charge carriers along with the efficient electron transfer path from the CB of TiO_2 to the Ni foam substrate (Table 2).

3.2. Energy storage applications of PI

3.2.1 Batteries. Among the various polymeric electrode materials, PI and its derivatives are considered to be very promising.[20,94] As Kovac and coworkers reported in the early 1990s, the carbonyl groups in PI show excellent reversibility owing to the fast kinetics of the enolization reaction,[95,96] which makes the intercalation and deintercalation of metal cations possible through redox reactions.[97] The electrochemical redox reaction of PI with Li^+ is displayed in Fig. 9(a).[98] Theoretically, PI has four carboxyl groups per repeating unit, thereby ensuring a high redox potential ($\sim$3 V *vs.* Li/Li^+) and is capable of reacting with four metal cations per unit. However, when a redox reaction involving all four carboxyl groups occurs, charge repulsion and irreversible damage to the structure become inevitable. Thus, the first redox reaction mainly contributes to the overall capacity of batteries.[100,101] In order to overcome this limitation in the redox reaction, diverse strategies for introducing additional carbonyl groups or benzene rings with an unsaturated alkene moiety have been reported. Specifically, these large conjugated systems enable the super-lithiation phenomenon since a metal cation can be inserted into the additional functional group following the imide carbonyl unit.[102–104]

As a representative example, Raj and coworkers synthesized two types of PIs, perylene diimide-benzidine (PDI-Bz) and perylene diimide-urea (PDI-Ur).[105] PDI-Ur has an additional conjugated carbonyl group in the imide region, thereby

Table 2 Representative examples of PI-based photoelectrochemical cells

Materials	Applications	Role of PI	Photoelectrochemical efficiency	Ref.
PI/TiO_2/CdSe	—	Charge separation	Photo-to-electron conversion efficiency = 8%	90
Vertically oriented TiO_2 nanotube arrays	—	Charge separation	Photo-to-electron conversion efficiency = 64.5%	92
PI/GO composites	Electrochromic materials	Matrix	Electrochromic coloration efficiency of C-0.5 = 157.36 cm^2 C^{-1}	91
Nano-TiO_2/PI/Ni foam photoanode	Degradation of methylene blue	Charge separation	Photoelectrocatalytic efficiency = 98.8%	93
PI/CdS composite	Enzyme biosensor	Charge separation and transfer	Correlation coefficient of hypoxanthine = 0.995	99

PI, polyimide; GO, graphene oxide; TiO_2, titanium dioxide; CdSe, cadmium selenide; CdS, cadmium sulphide.

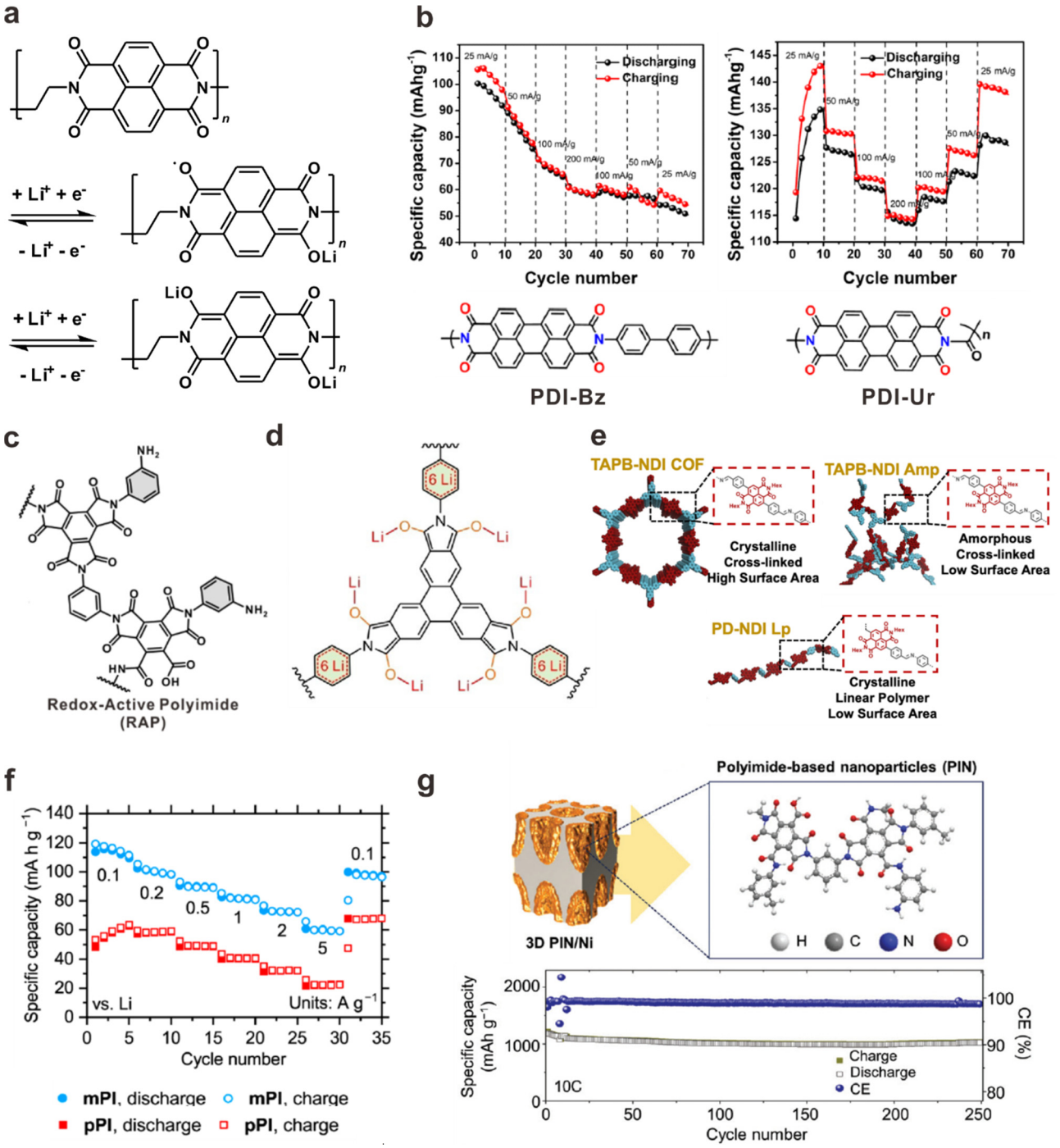

Fig. 9 (a) Electrochemical redox reactions of PI with Li^+. Reproduced with permission from ref. 99, copyright 2016, The Royal Society of Chemistry. (b) Rate capability performance (*vs.* Li^+/Li) of PDI-Bz and PDI-Ur. Reprinted with permission from ref. 105, copyright 2020 American Chemical Society. (c) The structure of redox-active PI microparticles. Reproduced with permission from ref. 106, copyright 2022, Elsevier. (d) Lithiation of a PIC-Ph anode material. Reproduced with permission from ref. 69, copyright 2021, John Wiley & Sons, Inc. (e) The morphology of the TAPB-naphthalene diimide (NDI) COF, TAPB-NDI Amp and PD-NDI Np. Reprinted with permission from ref. 113, copyright 2021 American Chemical Society. (f) High-rate capabilities of *m*PI and *p*PI in Li-based cells. Reprinted with permission from ref. 114, copyright 2021 American Chemical Society. (g) A schematic illustration and the capacity and CE of a 3D PIN/Ni electrode at various C-rates. Reproduced with permission from ref. 115, copyright 2021, The Royal Society of Chemistry.

enabling the additional exchange of one electron between oxygen and a metal ion. As a result, PDI-Ur contains five metal ions per unit cell, producing an excellent electrode performance when used as a cathode material (Fig. 9(b)). Specifically, PDI-Ur has two-fold higher lithiation capacity retention and 1.5-fold higher sodiation capacity retention than PDI-Bz.

Similarly, PI-based microparticles have been prepared *via* hydrothermal polymerization and applied as anode materials

in lithium-ion batteries (Fig. 9(c)).[106] The efficacy of this strategy was verified through cross-linking between *m*-phenylenediamine as a redox-active small molecule and poly(acrylic acid) as the binder. The imide and amic acid groups delivered 300 mA h g^{-1} due to the benzene ring in the PI structure. Thermal cross-linking between the *m*-phenylenediamine moiety and the poly(acrylic acid) binder enhanced the performance by three times (900 mA h g^{-1}) *via* the Li-ion inducing effect and the LUMO level. It is of note that this simple amide cross-linking strategy with a binder and the surface of PI microparticles enhanced not only stability but also the reaction kinetics.

Meanwhile, the morphology of PI also significantly influences the electrochemical performance. For example, nanosheet-type PI electrodes possess more active sites in contact with the electrolyte, resulting in improved capacity and rate performance.[107–109] Besides, 2D and 3D PIs with high porosity and crystallinity (*e.g.*, COFs) can efficiently transport metal cations of various sizes and charges due to their increased surface area and tunable pore size, thereby achieving high specific capacitance.[110–112] As a representative example, we presented highly crystalline PI-based COFs (PICs) for use as anode materials in Li-ion batteries (Fig. 9(d)).[69] PIC-Ph synthesized from triphenylene-2,3,6,7,10,11-hexacarboxylic acid in combination with *p*-phenylenediamine delivered a specific capacity of 691.9 mA h g^{-1} at 1.0C with long cycling stability for 200 cycles. The high-performance using PI was attributed to the following process: the redox-active carbonyl group of the imide bond is firstly oxidized by lithiation with 12 Li ions, followed by three benzene units reacting with 6 Li ions each, resulting in a total of 30 Li ions per unit cell.

Although it is commonly known that porous COF structures are advantageous for electrode performance, Jhulki *et al.* demonstrated that microscopic morphological differences can also play an important role. They synthesized various types of PIs derived from naphthalene diimides (NDIs), including an amorphous form, a linear form (PD-NDI Lp) and a 2D COF (TAPB-NDI COF) (Fig. 9(e)).[117] When applying them as the cathode material, TAPB-NDI COF exhibited the best charge/discharge performance at C/20 current rates.

Interestingly, however, PD-NDI Lp displayed overall higher gravimetric capacity and superior specific capacity retention at higher discharge rates compared to TAPB-NDI. When the discharge rate was increased from C/20 to C/2, the efficiency of TAPB-NDI dropped from 95% to 50%, while PD-NDI Lp retained 85% of its efficiency. In the case of TAPB-NDI, the efficiency was significantly reduced because the diffusion rate of Li ions through the pores was insufficient for the fast cycling rate. Scanning electron microscopy revealed clumped conductive additive particles that were the smallest in PD-NDI Lp, so the Li^+ diffusion distance is the shortest. In addition, PD-NDI Lp showed excellent adhesion to the current collector without noticeable cracks, resulting in excellent electrode performance even at high discharge rates.

In a similar vein, Kapaev and coworkers reported the effect of spatially arranging the imide units in PI-based cathode materials prepared by using *m*-phenylenediamine or *p*-phenylenediamine as the building block (Fig. 9(f)).[118] *m*-PI had a higher specific surface area and smaller particle size compared to the *p*-isomer prepared from *p*-phenylenediamine, which consequentially reduced the diffusion path of the metal cations. As a result, *m*-PI showed larger capacity and better high-speed performance compared to *p*-isomer. Moreover, the redox potential of *m*-PI is higher than that of *p*-isomer due to the spatial arrangement of the adjacent imide units that make the chelation of metal cations energetically and relatively more favourable.

Kim's group reported a hybrid anode comprising a 3D Ni scaffold covered with PI-based nanoparticles synthesized by lithographic fabrication (Fig. 9(g)).[119] PI-based nanoparticles containing multi-ring carbonyl groups can be lithiated not only

Table 3 Representative examples of PI-based batteries

Materials	Role of PI	Discharge capacity	Capacity retention	Ref.
Perylenediimide-urea	Cathode	119 mA h g^{-1} at 0.025 A g^{-1} (*vs.* Li^+/Li, Na^+/Na)	>100% over 50 cycles at 0.025 A g^{-1} (*vs.* Li^+/Li) 78.7% over 50 cycles at 0.025 A g^{-1} (*vs.* Na^+/Na)	105
Perylene-based aromatic PIs	Cathode	129 mA h g^{-1} at 0.025 A g^{-1}	71.3% over 50 cycles at 0.025 A g^{-1}	113
PI derivative prepared from NTCDA	Cathode	145 mA h g^{-1} at 0.1C	80.3% after 1000 cycles at 0.5C	114
PI@Ketjenblack composite	Cathode	143 mA h g^{-1} at 100 mA g^{-1}	76% over 1000 cycles at 2 A g^{-1}	115
Tb-DANT-COF (COF derived from 1,3,5-triformylbenzene and DANT)	Cathode	123.7 mA h g^{-1} at 1.4C	80.1 mA h g^{-1} after 300 cycles at 3.4C	110
PI-based COF derived from *p*-phenylene diamine	Anode	691.9 mA h g^{-1} at 1.0C	99.1% at 1.0C for 200 cycles	69
Crystalline few-layer 2D PI	Anode	312 mA h g^{-1} at 0.1 A g^{-1} (*vs.* Na^+/Na)	95% capacity retention after 1100 cycles at 1.0 A g^{-1} (*vs.* Na^+/Na)	109
Multicarbonyl aromatic PI derivative	Anode	992 mA h g^{-1} at 0.1 A g^{-1}	465 mA h g^{-1} after 150 cycles at 0.5 A g^{-1}	97
PI Schiff base	Anode	627.8 mA h g^{-1} at 0.25 A g^{-1}	85.7% after 1600 cycles at 2 A g^{-1}	104
Hierarchical multicarbonyl PI derivative	Anode	1343.8 mA h g^{-1} at 0.1 A g^{-1} (*vs.* Li^+/Li) 275.8 mA h g^{-1} at 0.025 A g^{-1} (*vs.* Li^+/Li)	665.1 mA h g^{-1} over 50 cycles at 0.25 A g^{-1} (*vs.* Li^+/Li) 130 mA h g^{-1} over 100 cycles at 0.05 A g^{-1} (*vs.* Na^+/Na)	116

PI, polyimide; NTCDA, 1,4,5,8-naphthalenetetracarboxylic dianhydride; DANT, 2,7-diaminobenzo[*lmn*][3,8]phenanthroline-1,3,6,8(2*H*,7*H*)-tetraone; COF, covalent organic framework.

to the terminal carboxylic acid group and carbonyl group but also to the C=C bond of the benzene ring. Therefore, 50 Li ions per repeating unit could be reversibly inserted and dissociated, thus increasing the theoretical capacity to 1460 mA h g^{-1}. Meanwhile, porous Ni was introduced as a conductive 3D support to increase electrical conductivity and improve hardness. This hybrid anode showed a fast electrochemical reaction rate because electrons and ions in the anode could move effectively and pass through the porous network structure. As a result, even at 10C, capacity retention of 82.8% for 250 cycles and a high reversible capacity of 1260 mA h g^{-1} were obtained by enabling efficient superlithiation. This suggests that fast charging and discharging even at a speed of up to 400C is feasible for use in high-speed charging hybrid electric vehicle systems (Table 3).

3.2.2 Supercapacitors. Due to its remarkable structural stability, mechanical strength and electrochemical activity, PI is considered a promising supercapacitor electrode material that can improve the electric double-layer capacitance and/or pseudocapacitance of a supercapacitor system.[20,120,121] For the former, PI is mainly utilised as a building block that can be converted into a porous structure to increase the energy density. For example, Kim's group reported laser-induced graphene patterning on fluorinated PIs.[122] The C–O, C=O and N–C bonds in the PI film were broken by the laser irradiation, while the oxygen and nitrogen components were significantly reduced, resulting in the formation of a porous 3D network structure. However, because the strategy is not related to the redox properties of PI, the focus was more on the application of PI as a pseudocapacitor electrode that can store energy through reversible faradaic reactions. Since PI can store and release energy through association/disassociation between the imide groups and metal cations, it has a high theoretical capacity.

Lin and coworkers synthesized π-conjugated PI-based organic electrodes with different lengths of alkyl chains to achieve a high-rate capability and a long lifetime (Fig. 10(a)).[123] The π-conjugated unit is advantageous for improving the electronic conductivity, while its stability in aqueous electrolyte is improved after polymerization. A fabricated asymmetric supercapacitor

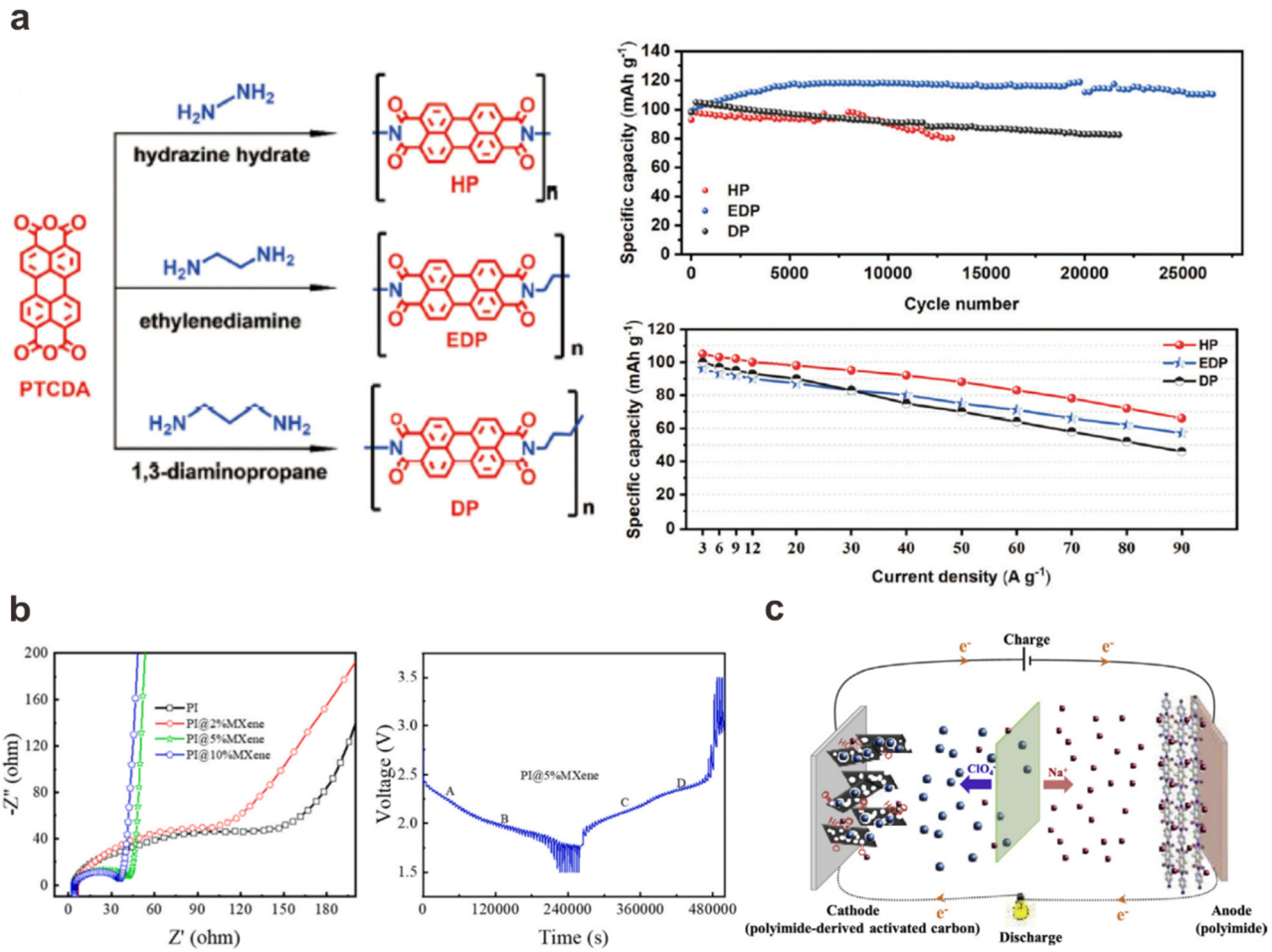

Fig. 10 (a) A scheme of π-conjugated PIs comprising different lengths of alkyl chains and the effect of the latter on cycling performance and rate capability. Reproduced with permission from ref. 123, copyright 2022, John Wiley & Sons, Inc. (b) Electrochemical impedance spectra and galvanostatic intermittent titration of PI@MXene. Reproduced with permission from ref. 124, copyright 2022, Elsevier. (c) A schematic illustration of the charging mechanism of a hybrid sodium-ion capacitor. Reproduced with permission from ref. 125, copyright 2018, Elsevier.

Table 4 Representative examples of PI-based supercapacitors

Materials	Role of PI	Capacity or capacitance	Capacity retention	Energy density	Ref.
Pyromellitic dianhydride-based PI	Anode and cathode	11 F g^{-1} at a current density of 0.4 A g^{-1}	72.4% after 1000 cycles at 0.4 A g^{-1}	66 W h kg^{-1} at a power density of 196 W kg^{-1}	125
Large π-conjugated PIs	Electrode	412 F g^{-1} at a scan rate of 1 mV s^{-1}	88% after 10 000 cycles at 3 A g^{-1}	10.2 W h kg^{-1} at a power density of 189 W kg^{-1}	123
PI@MXene porous organic cathode	Cathode	97 mA h g^{-1} at a current density of 0.5 A g^{-1}	—	—	124
PI deposited on CNT nanofibers	Anode	32.8 F g^{-1} at 0.74 mA cm^{-2}	96.4% after 2000 cycles	36.4 μ W h cm^{-2} at power density of 0.78 mW cm^{-2}	126
Porous PI nanofibers	Anode	107.3 mA h g^{-1} at 2.5 A g^{-1}	110% after 6000 cycles	103.2 W h kg^{-1} at 20 A g^{-1}	127

PI, polyimide; CNT, carbon nanotube.

based on hydrazine hydrate-derived PI without an alkyl chain revealed an excellent rate capability with a specific charge capacity of 92 mA h g^{-1} at a current density of 40 A g^{-1}. However, PIs derived from ethylenediamine and 1,3-diaminopropane with an alkyl chain exhibited better cycling stability but inferior rate capability compared to hydrazine hydrate-derived PI. In the case of PI comprising long alkyl chains, although the π-conjugation imide bonds are spatially blocked and thus the power capability is reduced, it has a more negative n-doping potential, thereby improving its stability against chemical degradation.

Min and coworkers fabricated a PI@MXene hybrid electrode incorporating titanium carbide (a low-dimensional nanomaterial with excellent electrochemical performance) to increase the conductivity of PI (Fig. 10(b)).[124] The combination of the porous PI coating and few-layered MXene with lamellar morphology creates multiple channels for electron and ion transport both inside and outside the material. Through the results of EIS and galvanostatic intermittent titration technique, PI@MXene featured a higher Li-ion diffusion coefficient and lower impedance compared to bare PI. In conclusion, the contribution rate of capacitive behaviour increased to 69% and 83% at scan rates of 1 and 2 mV s^{-1}, respectively, confirming that the pseudocapacitive effect was enhanced.

Zhao's group reported a hybrid Na-ion capacitor containing a PI anode and a PI-derived carbon cathode (Fig. 10(c)):[125] the former fabricated through a two-step enolization reaction enables the reversible insertion of Na ions whereas the latter fabricated through heat treatment has a high specific surface area and interconnected form advantageous for charge storage through an electric double layer mechanism. During the charging of a hybrid capacitor composed of these two electrodes, Na ions are reversibly inserted into the anode while reversible adsorption of perchlorate anions and release of Na ions occur at the cathode. It showed a high energy density of 66 W h kg^{-1} at a power density of 196 W kg^{-1}, suggesting that high-performance capacitors can be manufactured even with a single polymer (Table 4).

4. Summary and outlook

In this review, we presented the design, as well as the physical and chemical characteristics and electrochemical activities, of robust PIs for energy conversion and storage applications. In addition to the diverse synthetic methods with variable combinations of precursors, PIs have been developed with various topologies, from 1D to 3D, as well as amorphous to crystalline and porous structures, through controlling the reaction conditions such as the temperature, solvent(s) and/or precursor(s). In particular, from the standpoint of designing redox-active PIs, the energy band level to determine whether it can be used to harvest visible-light energy and the number of electroactive sites (the reaction of carbonyl groups with metal cations) are easily tuneable. Moreover, PI-based nanocomposites with other supporting nanomaterials can improve the photochemical and electrochemical activities as well (Fig. 11).

Novel synthetic protocols and recent advances in electrochemical analysis techniques have broaden the utilisation of PI for energy conversion and storage. Although diverse synthetic methods beyond traditional ones have been developed with the surge of novel application fields, many of them still possess limitation in use of toxic organic solvents, and high temperature. In this context, new approaches for developing eco-friendly synthetic method for PI are highly desirable such as hydrothermal synthesis and solid-state mechanochemical synthesis to alleviate aforementioned issues. Furthermore, nanostructures with controlled assembly should be considered as a new dimension for fine tuning the electrochemical properties of PI necessary for the device applications. More in-depth understanding on how each functionality of PI influences on the nanoscale assembly, which, in turn, modulates the performance of the devices is suggested. In view of the application fields, an increase of voltage window and charging/discharging rate should be considered carefully as well as the capacity when designing new functional monomers for energy storage and conversion devices. Beyond current subjects of redox-active PIs, there are significant needs for the development as flexible display substrate and next-generation network materials based on the excellent properties of high-performance PI. As such, we envision that robust PI can offer a new opportunity as a promising all-in-one material that can be used as not only redox-active material but also flexible and robust substrate. These new future directions will gear the development of the PI for advanced materials for future electronics.

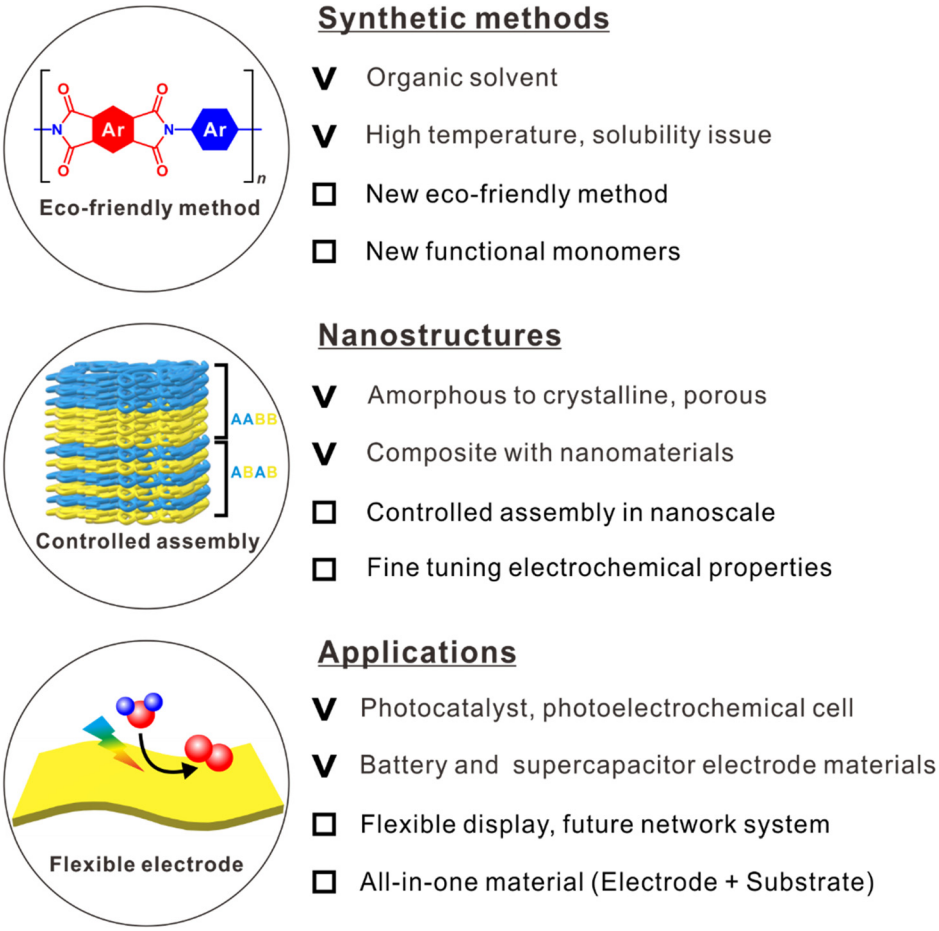

Fig. 11 Schematic illustration of the outlook for the development of PI.

Author contributions

All authors contributed to the discussion of contents and the editing of the manuscript prior to submission.

Conflicts of interest

There are no conflicts to declare.

Acknowledgements

This work was supported by the National Research Foundation of Korea (NRF-2021M3H4A1A04092882 and NRF-2022R1F1 A1074498).

References

1 B. C.-K. Tee, A. Chortos, A. Berndt, A. K. Nguyen, A. Tom, A. McGuire, Z. C. Lin, K. Tien, W.-G. Bae, H. Wang, P. Mei, H.-H. Chou, B. Cui, K. Deisseroth, T. N. Ng and Z. Bao, *Science*, 2015, **350**, 313–316.
2 H. Ling, S. Liu, Z. Zheng and F. Yan, *Small Methods*, 2018, **2**, 1800070.
3 C. Wang, H. Dong, W. Hu, Y. Liu and D. Zhu, *Chem. Rev.*, 2012, **112**, 2208–2267.
4 L. Huang, P. Jiang, D. Wang, Y. Luo, M. Li, H. Lee and R. A. Gerhardt, *Sens. Actuators, B*, 2014, **197**, 308–313.
5 S. Choi, H. Lee, R. Ghaffari, T. Hyeon and D.-H. Kim, *Adv. Mater.*, 2016, **28**, 4203–4218.
6 Y. Yang, X. Yang, Y. Tan and Q. Yuan, *Nano Res.*, 2017, **10**, 1560–1583.
7 X. Chen, X. Han and Q.-D. Shen, *Adv. Electron. Mater.*, 2017, **3**, 1600460.
8 J.-H. Bahk, H. Fang, K. Yazawa and A. Shakouri, *J. Mater. Chem. C*, 2015, **3**, 10362–10374.
9 P. M. Hergenrother, *High Perform. Polym.*, 2003, **15**, 3–45.
10 J. Nam, Y. Lee, W. Choi, C. S. Kim, H. Kim, J. Kim, D.-H. Kim and S. Jo, *Adv. Energy Mater.*, 2016, **6**, 1601269.
11 S. Chu, Y. Wang, Y. Guo, J. Feng, C. Wang, W. Luo, X. Fan and Z. Zou, *ACS Catal.*, 2013, **3**, 912–919.
12 Y. Shiraishi, S. Kanazawa, Y. Kofuji, H. Sakamoto, S. Ichikawa, S. Tanaka and T. Hirai, *Angew. Chem., Int. Ed.*, 2014, **53**, 13454–13459.
13 Y.-X. Lin, W.-J. Feng, J.-J. Zhang, Z.-H. Xue, T.-J. Zhao, H. Su, S.-I. Hirano, X.-H. Li and J.-S. Chen, *Angew. Chem., Int. Ed.*, 2018, **57**, 12563–12566.
14 X. Wang, X. Zhao, Y. Zhao, H.-Q. Tan, Z. Du, Q. Shang, T. Qiu and W. Ho, *Phys. Chem. Chem. Phys.*, 2019, **21**, 17163–17169.
15 T. K. T. Tu, S. A. Salma, M. Jeong, J. H. Kim, Y. T. Jeong, Y.-S. Gal and K. T. Lim, *Macromol. Res.*, 2021, **29**, 735–742.
16 J. Kosco, M. Bidwell, H. Cha, T. Martin, C. T. Howells, M. Sachs, D. H. Anjum, S. Gonzalez Lopez, L. Zou, A. Wadsworth, W. Zhang, L. Zhang, J. Tellam, R. Sougrat, F. Laquai, D. M. DeLongchamp, J. R. Durrant and I. McCulloch, *Nat. Mater.*, 2020, **19**, 559–565.
17 C. Yang, B. C. Ma, L. Zhang, S. Lin, S. Ghasimi, K. Landfester, K. A. I. Zhang and X. Wang, *Angew. Chem., Int. Ed.*, 2016, **55**, 9202–9206.

18 Y. Liu, Z. Liao, X. Ma and Z. Xiang, *ACS Appl. Mater. Interfaces*, 2018, **10**, 30698–30705.
19 H. Yang, X. Li, R. S. Sprick and A. I. Cooper, *Chem. Commun.*, 2020, **56**, 6790–6793.
20 Z. Song, H. Zhan and Y. Zhou, *Angew. Chem., Int. Ed.*, 2010, **49**, 8444–8448.
21 K. Amin, L. Mao and Z. Wei, *Macromol. Rapid Commun.*, 2019, **40**, 1800565.
22 H. Wang, S. Yuan, D. Ma, X. Huang, F. Meng and X. Zhang, *Adv. Energy Mater.*, 2014, **4**, 1301651.
23 F. Xu, J. Xia, W. Shi and S. Cao, *Mater. Chem. Phys.*, 2016, **169**, 192–197.
24 M. T. Bogert and R. R. Renshaw, *J. Am. Chem. Soc.*, 1908, **30**, 1135–1144.
25 R. W. Snyder, B. Thomson, B. Bartges, D. Czerniawski and P. C. Painter, *Macromolecules*, 1989, **22**, 4166–4172.
26 S. V. Vinogradova, Y. S. Vygodskii, V. D. Vorob'ev, N. A. Churochkina, L. I. Chudina, T. N. Spirina and V. V. Korshak, *Polym. Sci. U.S.S.R.*, 1974, **16**, 584–589.
27 R. A. Meyers, *J. Polym. Sci., Part A-1: Polym. Chem.*, 1969, **7**, 2757–2762.
28 P. S. Carleton, W. J. Farrissey and J. S. Rose, *J. Appl. Polym. Sci.*, 1972, **16**, 2983–2989.
29 S. Chu, Y. Wang, Y. Guo, P. Zhou, H. Yu, L. Luo, F. Kong and Z. Zou, *J. Mater. Chem.*, 2012, **22**, 15519.
30 L. Lin, P. Ye, C. Cao, Q. Jin, G.-S. Xu, Y.-H. Shen and Y.-P. Yuan, *J. Mater. Chem. A*, 2015, **3**, 10205–10208.
31 T. Rensch, S. Fabig, S. Grätz and L. Borchardt, *ChemSusChem*, 2022, **15**, e202101975.
32 J. Chiefari, B. Dao, A. M. Groth and J. H. Hodgkin, *High Perform. Polym.*, 2003, **15**, 269–279.
33 B. Baumgartner, M. J. Bojdys and M. M. Unterlass, *Polym. Chem.*, 2014, **5**, 3771–3776.
34 B. Baumgartner, M. Puchberger and M. M. Unterlass, *Polym. Chem.*, 2015, **6**, 5773–5781.
35 T. Kim, B. Park, K. M. Lee, S. H. Joo, M. S. Kang, W. C. Yoo, S. K. Kwak and B.-S. Kim, *ACS Macro Lett.*, 2018, **7**, 1480–1485.
36 N. Akiya and P. E. Savage, *Chem. Rev.*, 2002, **102**, 2725–2750.
37 M. Uematsu and E. U. Frank, *J. Phys. Chem. Ref. Data*, 1980, **9**, 1291–1306.
38 W. L. Marshall and E. U. Franck, *J. Phys. Chem. Ref. Data*, 1981, **10**, 295–304.
39 L. Yi, W. Huang and D. Yan, *J. Polym. Sci., Part A: Polym. Chem.*, 2017, **55**, 533–559.
40 U. Yildiko and A. A. Tanriverdi, *Bull. Korean Chem. Soc.*, 2022, **43**, 822–835.
41 K. Tanaka, H. Kita, M. Okano and K. Okamoto, *Polymer*, 1992, **33**, 585–592.
42 S.-H. Hsiao and T.-L. Huang, *J. Polym. Res.*, 2004, **11**, 9–21.
43 S. V. Kumar, H.-C. Yu, J. Choi, K. Kudo, Y.-H. Jang and C.-M. Chung, *J. Polym. Res.*, 2011, **18**, 1111–1117.
44 Y. Yin, J. Fang, T. Watari, K. Tanaka, H. Kita and K. Okamoto, *J. Mater. Chem.*, 2004, **14**, 1062.
45 Y. Sutou, Y. Yin, Z. Hu, S. Chen, H. Kita, K.-I. Okamoto, H. Wang and H. Kawasato, *J. Polym. Sci., Part A: Polym. Chem.*, 2009, **47**, 1463–1477.
46 P. K. Tapaswi, M.-C. Choi, S. Nagappan and C.-S. Ha, *J. Polym. Sci., Part A: Polym. Chem.*, 2015, **53**, 479–488.
47 D.-J. Liaw, B.-Y. Liaw, P.-N. Hsu and C.-Y. Hwang, *Chem. Mater.*, 2001, **13**, 1811–1816.
48 D. Liaw, P. Hsu, W. Chen and B. Liaw, *Macromol. Chem. Phys.*, 2001, **202**, 1483–1487.
49 D. Sahadeva Reddy, C.-H. Chou, C.-F. Shu and G.-H. Lee, *Polymer*, 2003, **44**, 557–563.
50 Y.-H. Kim, H.-S. Kim and S.-K. Kwon, *Macromolecules*, 2005, **38**, 7950–7956.
51 K. Zeng, Q. Guo, S. Gao, D. Wu, H. Fan and G. Yang, *Macromol. Res.*, 2012, **20**, 10–20.
52 S. Bong, H. Yeo, B.-C. Ku, M. Goh and N.-H. You, *Macromol. Res.*, 2018, **26**, 85–91.
53 M. Jikei and M. Kakimoto, *J. Polym. Sci., Part A: Polym. Chem.*, 2004, **42**, 1293–1309.
54 C.-M. Leu, Y.-T. Chang, C.-F. Shu, C.-F. Teng and J. Shiea, *Macromolecules*, 2000, **33**, 2855–2861.
55 C.-M. Leu, C.-F. Shu, C.-F. Teng and J. Shiea, *Polymer*, 2001, **42**, 2339–2348.
56 K. Yamanaka, M. Jikei and M. Kakimoto, *Macromolecules*, 2000, **33**, 1111–1114.
57 K. Yamanaka, M. Jikei and M. Kakimoto, *Macromolecules*, 2000, **33**, 6937–6944.
58 K. Yamanaka, M. Jikei and M. Kakimoto, *Macromolecules*, 2001, **34**, 3910–3915.
59 S. Chu, Y. Pan, Y. Wang, H. Zhang, R. Xiao and Z. Zou, *J. Mater. Chem. A*, 2020, **8**, 14441–14462.
60 J. Hao, M. Jikei and M. Kakimoto, *Macromolecules*, 2002, **35**, 5372–5381.
61 D. Tian, H.-Z. Zhang, D.-S. Zhang, Z. Chang, J. Han, X.-P. Gao and X.-H. Bu, *RSC Adv.*, 2014, **4**, 7506.
62 C. Zhang, X. Yang, W. Ren, Y. Wang, F. Su and J.-X. Jiang, *J. Power Sources*, 2016, **317**, 49–56.
63 J. K. Park, *Bull. Korean Chem. Soc.*, 2017, **38**, 153–154.
64 Q. Wang, J. Zhang, Y. Yu, Y. Dan and L. Jiang, *New J. Chem.*, 2018, **42**, 12205–12211.
65 B. B. Narzary, B. C. Baker, N. Yadav, V. D'Elia and C. F. J. Faul, *Polym. Chem.*, 2021, **12**, 6494–6514.
66 Q. Fang, Z. Zhuang, S. Gu, R. B. Kaspar, J. Zheng, J. Wang, S. Qiu and Y. Yan, *Nat. Commun.*, 2014, **5**, 4503.
67 Q. Fang, J. Wang, S. Gu, R. B. Kaspar, Z. Zhuang, J. Zheng, H. Guo, S. Qiu and Y. Yan, *J. Am. Chem. Soc.*, 2015, **137**, 8352–8355.
68 Y. Zhang, Z. Huang, B. Ruan, X. Zhang, T. Jiang, N. Ma and F. Tsai, *Macromol. Rapid Commun.*, 2020, **41**, 2000402.
69 T. Kim, S. H. Joo, J. Gong, S. Choi, J. H. Min, Y. Kim, G. Lee, E. Lee, S. Park, S. K. Kwak, H. Lee and B. Kim, *Angew. Chem., Int. Ed.*, 2022, **61**, e202113780.
70 J. Maschita, T. Banerjee, G. Savasci, F. Haase, C. Ochsenfeld and B. V. Lotsch, *Angew. Chem., Int. Ed.*, 2020, **59**, 15750–15758.
71 X. Liang, G. Wang, T. Huo, X. Dong, G. Wang, H. Ma, H. Liang and X. Zhang, *Catal. Commun.*, 2019, **123**, 44–48.
72 Y. Xu, N. Mao, C. Zhang, X. Wang, J. Zeng, Y. Chen, F. Wang and J.-X. Jiang, *Appl. Catal., B*, 2018, **228**, 1–9.
73 Z.-A. Lan, W. Ren, X. Chen, Y. Zhang and X. Wang, *Appl. Catal., B*, 2019, **245**, 596–603.
74 H. Heng, J. Yang, Y. Yin, P. Meng and X. Liu, *Catal. Today*, 2020, **340**, 225–235.
75 S. Chu, Y. Wang, C. Wang, J. Yang and Z. Zou, *Int. J. Hydrogen Energy*, 2013, **38**, 10768–10772.
76 H. Wang, L. Zhang, Z. Chen, J. Hu, S. Li, Z. Wang, J. Liu and X. Wang, *Chem. Soc. Rev.*, 2014, **43**, 5234.
77 Y.-P. Yuan, L.-W. Ruan, J. Barber, S. C. Joachim Loo and C. Xue, *Energy Environ. Sci.*, 2014, **7**, 3934–3951.
78 H. Li, Y. Zhou, W. Tu, J. Ye and Z. Zou, *Adv. Funct. Mater.*, 2015, **25**, 998–1013.
79 S. J. A. Moniz, S. A. Shevlin, D. J. Martin, Z. X. Guo and J. Tang, *Energy Environ. Sci.*, 2015, **8**, 731–759.
80 J. Low, J. Yu, M. Jaroniec, S. Wageh and A. A. Al-Ghamdi, *Adv. Mater.*, 2017, **29**, 1601694.
81 T. Yan, M. Li, X. Wang, M. Sun, H. Liu, Q. Wei, W. Xu and B. Du, *Appl. Surf. Sci.*, 2015, **340**, 102–112.
82 Y. Hu, X. Hao, Z. Cui, J. Zhou, S. Chu, Y. Wang and Z. Zou, *Appl. Catal., B*, 2020, **260**, 118131.
83 Q. Guo, H. Li, Q. Zhang and Y. Zhang, *Appl. Catal., B*, 2018, **229**, 192–203.
84 X. Zhao, X. Wang, J. Zhang and X. Yi, *Chem. – Asian J.*, 2019, **14**, 422–430.
85 X. Zhao, X. Yi, X. Wang, W. Chu, S. Guo, J. Zhang, B. Liu and X. Liu, *Appl. Surf. Sci.*, 2020, **502**, 144187.
86 Y. Kofuji, S. Ohkita, Y. Shiraishi, H. Sakamoto, S. Tanaka, S. Ichikawa and T. Hirai, *ACS Catal.*, 2016, **6**, 7021–7029.
87 Y. Kofuji, Y. Isobe, Y. Shiraishi, H. Sakamoto, S. Tanaka, S. Ichikawa and T. Hirai, *J. Am. Chem. Soc.*, 2016, **138**, 10019–10025.
88 Y. Kofuji, S. Ohkita, Y. Shiraishi, H. Sakamoto, S. Ichikawa, S. Tanaka and T. Hirai, *ACS Sustainable Chem. Eng.*, 2017, **5**, 6478–6485.
89 J. Zhou, Y. Lei, C. Ma, W. Lv, N. Li, Y. Wang, H. Xu and Z. Zou, *Chem. Commun.*, 2017, **53**, 10536–10539.
90 C. Wang, Z. Huang, X. Bai, N. Huang and B. Wang, *Pigm. Resin Technol.*, 2006, **35**, 132–136.

91 L. Ma, H. Niu, J. Cai, P. Zhao, C. Wang, X. Bai, Y. Lian and W. Wang, *Carbon*, 2014, **67**, 488–499.
92 X. Tong, P. Yang, Y. Wang, Y. Qin and X. Guo, *Nanoscale*, 2014, **6**, 6692–6700.
93 Y. Lei and J. Huo, *Res. Chem. Intermed.*, 2018, **44**, 6401–6418.
94 H. Yang, S. Liu, L. Cao, S. Jiang and H. Hou, *J. Mater. Chem. A*, 2018, **6**, 21216–21224.
95 W. Deng, Y. Shen, J. Qian and H. Yang, *Chem. Commun.*, 2015, **51**, 5097–5099.
96 A. Viehbeck, M. J. Goldberg and C. A. Kovac, *J. Electrochem. Soc.*, 1990, **137**, 1460–1466.
97 Z. Ba, Z. Wang, Y. Zhou, H. Li, J. Dong, Q. Zhang and X. Zhao, *ACS Appl. Energy Mater.*, 2021, **4**, 13161–13171.
98 Y. Zhang, Y. Wang, L. Wang, C.-M. Lo, Y. Zhao, Y. Jiao, G. Zheng and H. Peng, *J. Mater. Chem. A*, 2016, **4**, 9002–9008.
99 R. Li, C. Ye, X. Y. Zhang, N. B. Li and H. Q. Luo, *Sens. Actuators, B*, 2020, **314**, 128079.
100 L. Chen, W. Li, Y. Wang, C. Wang and Y. Xia, *RSC Adv.*, 2014, **4**, 25369–25373.
101 H. Wang, C.-J. Yao, H.-J. Nie, K.-Z. Wang, Y.-W. Zhong, P. Chen, S. Mei and Q. Zhang, *J. Mater. Chem. A*, 2020, **8**, 11906–11922.
102 J. Wu, X. Rui, C. Wang, W.-B. Pei, R. Lau, Q. Yan and Q. Zhang, *Adv. Energy Mater.*, 2015, **5**, 1402189.
103 S. Renault, V. A. Oltean, C. M. Araujo, A. Grigoriev, K. Edström and D. Brandell, *Chem. Mater.*, 2016, **28**, 1920–1926.
104 J. Wang, H. Yao, C. Du and S. Guan, *J. Power Sources*, 2021, **482**, 228931.
105 M. Ruby Raj, R. V. Mangalaraja, D. Contreras, K. Varaprasad, M. V. Reddy and S. Adams, *ACS Appl. Energy Mater.*, 2020, **3**, 240–252.
106 T. Kim, S. Choi, J. Ryu, Y. Kim, G. Lee, B.-S. Kim and S. Park, *Appl. Surf. Sci.*, 2022, **601**, 154220.
107 F. Wan, X.-L. Wu, J.-Z. Guo, J.-Y. Li, J.-P. Zhang, L. Niu and R.-S. Wang, *Nano Energy*, 2015, **13**, 450–457.
108 Q. Zhao, R. R. Gaddam, D. Yang, E. Strounina, A. K. Whittaker and X. S. Zhao, *Electrochim. Acta*, 2018, **265**, 702–708.
109 H. Duan, P. Lyu, J. Liu, Y. Zhao and Y. Xu, *ACS Nano*, 2019, **13**, 2473–2480.
110 D.-H. Yang, Z.-Q. Yao, D. Wu, Y.-H. Zhang, Z. Zhou and X.-H. Bu, *J. Mater. Chem. A*, 2016, **4**, 18621–18627.
111 R. van der Jagt, A. Vasileiadis, H. Veldhuizen, P. Shao, X. Feng, S. Ganapathy, N. C. Habisreutinger, M. A. van der Veen, C. Wang, M. Wagemaker, S. van der Zwaag and A. Nagai, *Chem. Mater.*, 2021, **33**, 818–833.
112 S. Kandambeth, V. S. Kale, O. Shekhah, H. N. Alshareef and M. Eddaoudi, *Adv. Energy Mater.*, 2022, **12**, 2100177.
113 M. Ruby Raj, R. V. Mangalaraja, G. Lee, D. Contreras, K. Zaghib and M. V. Reddy, *ACS Appl. Energy Mater.*, 2020, **3**, 6511–6524.
114 Z. Ba, Z. Wang, M. Luo, H. Li, Y. Li, T. Huang, J. Dong, Q. Zhang and X. Zhao, *ACS Appl. Mater. Interfaces*, 2020, **12**, 807–817.
115 C. Zhang, Y. Xu, K. He, Y. Dong, H. Zhao, L. Medenbach, Y. Wu, A. Balducci, T. Hannappel and Y. Lei, *Small*, 2020, **16**, 2002953.
116 J. Li, M. Luo, Z. Ba, Z. Wang, L. Chen, Y. Li, M. Li, H.-B. Li, J. Dong, X. Zhao and Q. Zhang, *J. Mater. Chem. A*, 2019, **7**, 19112–19119.
117 S. Jhulki, C. H. Feriante, R. Mysyk, A. M. Evans, A. Magasinski, A. S. Raman, K. Turcheniuk, S. Barlow, W. R. Dichtel, G. Yushin and S. R. Marder, *ACS Appl. Energy Mater.*, 2021, **4**, 350–356.
118 R. R. Kapaev, A. G. Scherbakov, A. F. Shestakov, K. J. Stevenson and P. A. Troshin, *ACS Appl. Energy Mater.*, 2021, **4**, 4465–4472.
119 Y. Ham, N. J. Fritz, G. Hyun, Y. B. Lee, J. S. Nam, I.-D. Kim, P. V. Braun and S. Jeon, *Energy Environ. Sci.*, 2021, **14**, 5894–5902.
120 B. Häupler, A. Wild and U. S. Schubert, *Adv. Energy Mater.*, 2015, **5**, 1402034.
121 Y. Zhao, J. Liu, D. Zheng, B. Wang, M. Hu, J. Sha and Y. Li, *Small*, 2018, **14**, 1702809.
122 M. Kim, M. G. Gu, H. Jeong, E. Song, J. W. Jeon, K.-M. Huh, P. Kang, S.-K. Kim and B. G. Kim, *ACS Appl. Energy Mater.*, 2021, **4**, 208–214.
123 Y. Zhao, S. Zhang, S. Xu, X. Li, Y. Zhang, Y. Xu, J. Zhou, H. Bi, F. Huang and T. Lin, *Macromol. Rapid Commun.*, 2022, **43**, 2200040.
124 X.-W. Huang, S.-Y. Liao, Y.-Z. Li, C.-S. Liu, W.-X. Cheng, C. Zhao, Y.-Z. Chen, Y.-D. Liu and Y.-G. Min, *J. Alloys Compd.*, 2022, **919**, 165559.
125 Q. Zhao, D. Yang, A. K. Whittaker and X. S. Zhao, *J. Power Sources*, 2018, **396**, 12–18.
126 G. Huang, Y. Zhang, L. Wang, P. Sheng and H. Peng, *Carbon*, 2017, **125**, 595–604.
127 M. Yang and W. J. Song, *J. Mater. Chem. A*, 2022, **10**, 17511–17519.